


Topological Anderson insulating phases in the long-range Su-Schrieffer-Heeger model

Hsiu-Chuan Hsu^{1,2,*} and Tsung-Wei Chen³

¹*Graduate Institute of Applied Physics, National Chengchi University, Taipei 11605, Taiwan*

²*Department of Computer Science, National Chengchi University, Taipei 11605, Taiwan*

³*Department of Physics, National Sun Yat-sen University, Kaohsiung 804, Taiwan*

 (Received 21 April 2020; revised 9 November 2020; accepted 10 November 2020; published 23 November 2020)

The long-range Su-Schrieffer-Heeger (SSH) model, in which the second nearest-neighbor hopping is taken into account, exhibits a topological phase diagram that contains winding numbers $w = 0, 1$, and 2 . In the clean system, the change in winding number stems from the band-touching phenomenon. In the presence of disorder, the renormalization of energy band and Fermi level results in the nonzero density of states in the energy gap. These midgap states cause the crossover phenomenon and the divergence of localization length at a critical disorder strength U_c in the finite SSH system. In this study, we numerically computed the mean winding number and localization length for the disordered SSH system. We find that the disorder is able to drive phase transitions between different mean winding numbers: $w = 0 \rightarrow 1, 0 \rightarrow 2, 1 \rightarrow 2$, and $2 \rightarrow 1$ in the weak disorder regime. By investigating the wave function distribution and the self-energy, the nonzero mean winding numbers correspond to the so-called topological Anderson insulating (TAI) phases. The finite size scaling for the mean winding number in the TAI phase is shown. For describing the phase transitions in the thermodynamic limit, we apply the criterion of band gap closure resulting from the broadening of energy band and Fermi level to determine the critical disorder strength. The critical disorder strength for self-consistent Born approximation (SCBA) U_c^{SCBA} and that for first Born approximation (FBA) U_c^{FBA} are numerically calculated. U_c^{SCBA} is found to match with U_c qualitatively. Nonetheless, SCBA indicates the different roles of band shifts and Fermi level broadening near the topological phase transitions. Band shift/Fermi level broadening is more dominant for the transitions from low-to-high/high-to-low winding number. Interestingly, for the transition from bulk insulator to TAI, U_c^{FBA} is quantitatively closer to U_c than U_c^{SCBA} as long as the renormalized band gap is zero within FBA.

DOI: [10.1103/PhysRevB.102.205425](https://doi.org/10.1103/PhysRevB.102.205425)

I. INTRODUCTION

The phenomena of localization of electronic wave function in random potential, now called Anderson localization, was proposed by Anderson in his pioneering work in 1958 [1]. The scaling theory of localization shows that, in low dimensions, all states are localized no matter how weak the disorder is [2,3]. As a result, in the thermodynamic limit, any low dimensional system is an insulator. In Ref. [4], the Anderson localization is directly observed in one-dimensional matter waves of rubidium-87 Bose-Einstein condensates with controlled disorder. On the other hand, when disorder is added to the system with energy band topology, some interesting phenomena arise. It is known that topological boundary modes are robust to disorder. In topological insulators with high Fermi level that both bulk and boundary modes transport, disorder plays a role that suppresses the bulk bands and leaves the boundary modes conduct [5]. Furthermore, in a normal insulator, disorder can drive the transition to a topological insulator. This is called the topological Anderson insulating (TAI) phase [6].

The TAI phase has been theoretically shown in several studies [6–11]. Li *et al.* [6] showed that, in a two-dimensional Bernevig–Hughes–Zhang (BHZ) model, disorder can lead to

band inversion and topological phase transition from normal to a nontrivial phase that carries quantized conductance. In the same system, Groth *et al.* [7] applied Born approximation to estimate the renormalization of gap parameter that leads to inverted bands. They conclude that the normal insulating and TAI phase boundary correspond to the crossing of a band edge. Although the name seems to suggest Anderson localization, the phase boundary actually exhibits a weak disorder transition. Guo *et al.* [8] also found that disorder transforms a normal insulator to a topological insulator in three dimensions. Similar to the conclusion drawn by Groth *et al.* [7], the weak-disorder boundary is the crossing of a band edge. Nonetheless, they found the TAI phase extends to a regime where energy broadening becomes significant and localization is the leading factor. Xu *et al.* [9] showed there are two kinds of TAI, the gapped and ungapped phases, in the two-dimensional BHZ model. In the gapped TAI, only edge states exist inside the energy gap. In the ungapped TAI, the bulk and edge states coexist, while the bulk states are localized by disorder. The latter is the counterpart of the extended TAI in three dimensions shown by Guo *et al.* [8].

On the other hand, Gergs *et al.* [12] showed that in the one-dimensional Kitaev model, the topology is stabilized by repulsive interaction and/or moderate disorder. Altland *et al.* [10,11] studied TAI phase transitions in multichannel Su-Schrieffer-Heeger (SSH) chains and found transitions

*hcjhsu@nccu.edu.tw

between different winding numbers. They utilized field theory within self-consistent Born approximation and two-parameter renormalization group flow to locate the phase boundaries for bulk/topological insulator (BI/TI) to TAI phases. It was shown in their studies that disorder induces crossover to the Anderson insulator before the phase transition, which was determined by delocalization and the half-integer winding number within SCBA. It is only until recently that the TAI phase has been observed experimentally [13]. A one-dimensional SSH model that preserves chiral symmetry was simulated in ultracold atoms. It was shown that the winding number (w) transitions from $w = 0$ to $w = 1$ as disorder strength increases. The experimental feasibility of the SSH model [13–15] makes it suitable for studying the interplay between band topology and disorder.

Therefore, as motivated by these investigations, it is worthwhile studying the rich phase diagram, the TAI phases, and the scattering mechanisms in the SSH model. In this study, to explore the nontrivial phases with high winding number in the presence of disorder, the long-range interaction, which is experimentally applicable [14], is included in the SSH model. TAI phases are shown in numerical simulations and the mechanisms are explained with Born approximation in the renormalized SSH system and theory of localization in the finite SSH system. For the renormalized system, the energy band is shifted and the Fermi level is broadened by the imaginary parts of the self-energy. This enables us to calculate the critical disorder strength by the closure of the band gap. In particular, we compare the phase boundary obtained from the divergence of localization length with the band closure within Born approximation. The crossover regions are observed in our numerical results, which correspond to the nonzero imaginary part of the self-energy in the renormalized SSH system. As proposed in several theoretical works, the BI-TAI transition, which corresponds to the $w = 0$ to $w = 1$ transition, is found. Furthermore, we find that the transition can go directly from $w = 0$ to $w = 2$ without crossing $w = 1$. The TI-TAI is the transition between two nontrivial insulating phases with different winding numbers. The transitions $w = 1 \rightarrow 2 \rightarrow 1$ and $w = 2 \rightarrow 1$ driven by disorder are found.

This paper is organized as follows. In Sec. II, the model Hamiltonian and the methods for characterizing the TAI phases are presented. The BI-TAI and TI-TAI transitions are discussed in Sec. III. We also present the thermodynamic limit for the fluctuation of winding number and conductance. In Sec. IV, the crossover regions and band closure are identified by self-energy within the Born approximation. The critical disorder strengths are calculated by using Born approximation and the comparison with the finite SSH system is discussed. Our conclusion is given in Sec. V.

II. LONG-RANGE SSH MODEL

The one-dimensional Su-Schrieffer-Heeger (SSH) Hamiltonian with long-range hopping that preserves chiral (sublattice) symmetry [16–19] is given by

$$H_0 = \sum_{i=0}^N J_0 C_{i,a}^\dagger C_{i,b} + J_1 C_{i+1,a}^\dagger C_{i,b} + J_2 C_{i+2,a}^\dagger C_{i,b} + \text{H.c.}, \quad (1)$$

where i is the lattice site, N is the length of the model, and $C_{i,a,b}^\dagger, C_{i,a,b}$ are the creation and annihilation operators on sublattices a, b on the i th unit cell. There are two types of nearest neighbor coupling. J_0 denotes the intracell coupling, while J_1 denotes the intercell coupling. In the momentum space, the SSH Hamiltonian is written as

$$H_0(k) = h_x(k)\sigma_x + h_y(k)\sigma_y, \quad (2)$$

where

$$\begin{aligned} h_x(k) &= J_0 + J_1 \cos k + J_2 \cos(2k), \\ h_y(k) &= J_1 \sin k + J_2 \sin(2k). \end{aligned} \quad (3)$$

$\sigma_{x,y}$ are Pauli matrices and act on the sublattices a, b . The lattice constant is taken to be unity. The eigenenergy is $E_\pm = \pm \sqrt{h_x^2 + h_y^2}$. Before directly calculating the topological phase, the phase diagram can be inferred by adiabatic connection [20,21].

The energy gap as a function of J_2/J_0 and J_1/J_0 is shown in Fig. 1(a). The phase diagram is asymmetric about $J_2 = 0$ due to the presence of the positive intracell term. The gap closing conditions are given by

$$1 + \frac{J_1}{J_0} \cos k_0 + \frac{J_2}{J_0} \cos(2k_0) = 0, \quad (4)$$

$$\frac{J_1}{J_0} \sin k_0 + \frac{J_2}{J_0} \sin(2k_0) = 0. \quad (5)$$

Equation (4) is satisfied when $k_0 = 0(\pi)$ and $J_0 \pm J_1 + J_2 = 0$, giving rise to the straight phase boundary with slope ∓ 1 and the interception at $J_2/J_0 = -1$, as shown in Fig. 1(a). Nonetheless, Eq. (5) is also satisfied by $J_1/J_2 = -2 \cos k_0$, which is plugged into Eq. (4) to obtain another condition $J_2/J_0 = 1$. As a result, these conditions give rise to the horizontal boundary of $J_2/J_0 = 1$ for $J_1/J_0 = [-2, 2]$, as shown in Fig. 1(a).

The geometrical origin of the topology lies in the sublattice pairing. In nontrivial topological phase, the bonding is formed between opposite sublattices from different lattice sites, i.e., sublattice a bonds with sublattice b at another site. This is referred to as the singlet pairing [13]. Quantitatively, this pairing is described by winding number denoted as w [13,16]. For $w = 1$, the average singlet pairing forms between the nearest neighbor, while, for $w = 2$, the average singlet pairing forms between the next nearest neighbor. In contrast, for trivial topology, the bonding is formed within the same lattice site.

To study the effect of disorder on the topological phases, the disordered intracell coupling is taken into account

$$H_U = \sum_{i=1}^N U_i C_{i,a}^\dagger C_{i,b}, \quad (6)$$

where U_i are given by the random number in the range $[-\frac{U}{2}, \frac{U}{2}]$, with U the disorder strengths in the unit of J_0 . For characterizing the topological phases in a disordered system, the winding numbers are computed numerically for the tight-binding Hamiltonian.

Here, we use the method proposed by [13,16] that applies for the chiral symmetric systems [13,18]. By defining $Q = P_+ - P_-$ and the chiral symmetry operators $S = S_+ - S_-$,

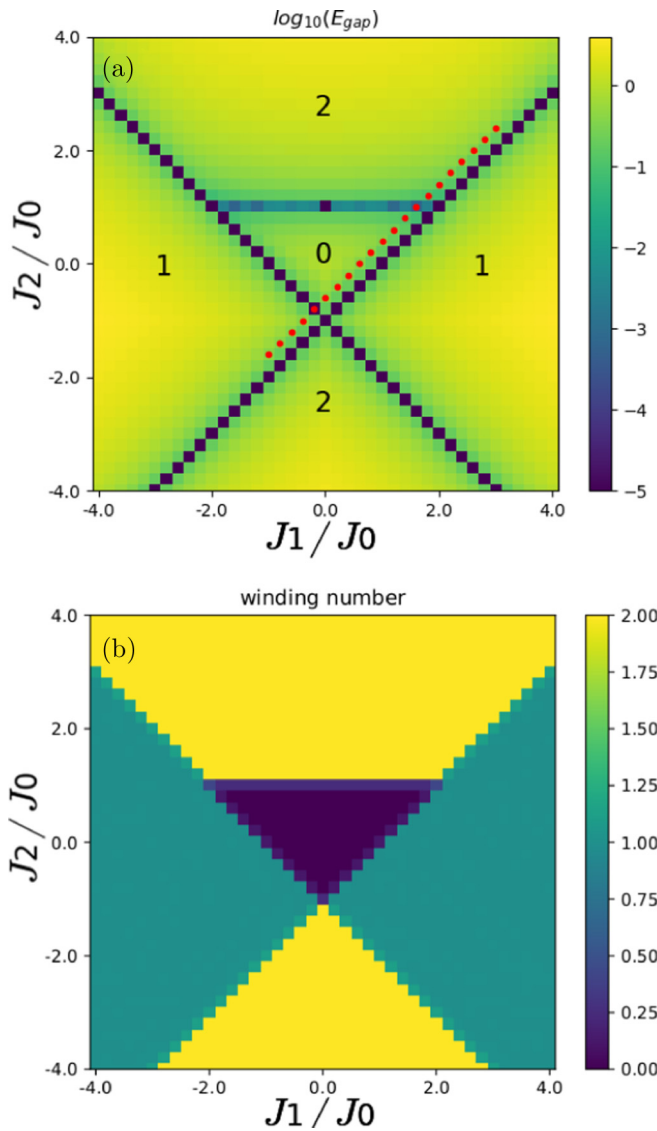


FIG. 1. (a) Energy gap. (b) The winding number as a function of J_1, J_2 . In (a), the winding numbers, annotated by the numbers on the plot, are inferred from adiabatic connection. The red dashed line is in the vicinity of the phase boundary, where the TAI phases are shown in Fig. 2. In (b), the length of chain is $N_x = 400$ for winding numbers. Comparing the two figures, the vanishing energy gap coincides with phase boundaries given by winding numbers.

where P_{\pm} are the projection operators that project to the positive or negative energy bands, S_{\pm} are the projection to sublattice a or b , the winding number is given by

$$w = -\text{Tr}_s\{Q_{-+}[X, Q_{+-}]\}, \quad (7)$$

where $Q_{+-} = S_+Q_S-$, $Q_{-+} = S_-Q_S+ = (Q_{+-})^{-1}$, X is the position operator, and $\text{Tr}_s(\dots)$ is the trace over the sublattices. This equation computes the local topological marker in real space [16,22]. We calculate the average over the central part as the winding number for a chain [13]. For disordered systems, the average over disorder configurations is performed as well. The winding number as a function of $J_1/J_0, J_2/J_0$ for the clean limit is shown in Fig. 1(b). The results coincide with that from adiabatic connection. However, the finite size effect

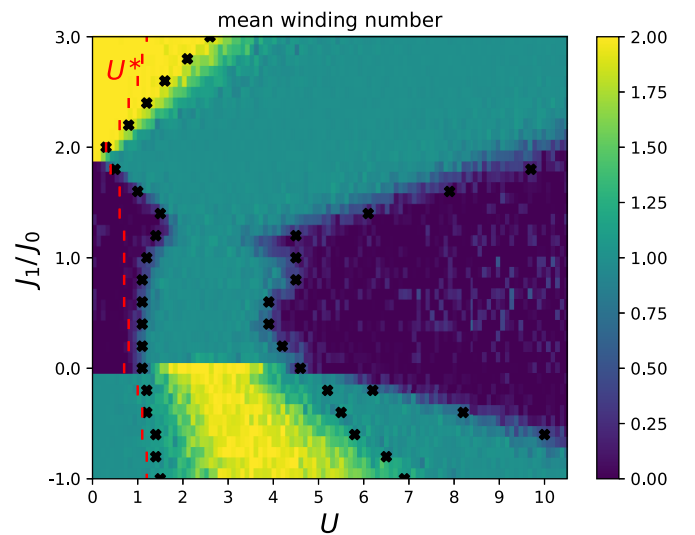


FIG. 2. Topological phases as a function of disorder strength and J_1/J_0 near the phase boundary, following the red dashed line in Fig. 1(a). The black crosses denote the peaks of the localization length. The red dashed line denotes U^* , at which the self-energy starts to acquire an imaginary part (discussed in Sec. IV).

in the tight-binding Hamiltonian could smooth out the phase boundaries. Therefore, the localization length, the peaks of which identify the topological phase transitions [16], must also be calculated.

To compute the localization length, the iterative Green's function method is adopted [23]. The localization length can be extracted from the Green's function [24,25]

$$\frac{2}{\lambda} = -\lim_{n \rightarrow \infty} \frac{1}{n} \text{Tr} \ln |G_{1n}|^2, \quad (8)$$

where n is the total number of sites of the SSH model and G_{1n} is the propagator connecting the first and the last slice of the system. A well-known challenge in this method is the vanishing small eigenvalues due to successive matrix multiplication. To overcome the numerical instability, we apply the method proposed in [24] that normalizes the Green's function regularly.

In the next section, we present the phase diagram driven by the disorder defined in Eq. (6) along the trajectory of the vicinity of the phase boundary [see Fig. 1(a)]. The mean winding number is calculated and its fluctuation with the length of the system is discussed.

III. TAI PHASES AND TRANSITIONS

We study the topological Anderson insulator (TAI) phase driven by the disordered intracell coupling, as shown in Eq. (6). The TAI phase transition is investigated near the phase boundaries in the clean limit. Fixing $J_0 = 1$ and $J_2 = J_1 - 0.94$, the mean winding numbers are plotted as a function of disorder strength and J_1/J_0 , as shown in Fig. 2.

The winding number in the clean limit is retained up to a critical disorder. As disorder strength increases, mean winding numbers change to another integer. In Fig. 2, two types of transitions are observed from this numerical result. The transition from bulk insulator (BI) to TAI is the transition from zero

mean winding number to a nonzero mean winding number. Such transition can be seen for $0 \leq J_1/J_0 < 2$ in Fig. 2. The transition from topological insulator (TI) to TAI is the transition between the two nontrivial topological phases. It occurs for $-1 \leq J_1/J_0 < 0$ and $2 \leq J_1/J_0 \leq 3$ at weak disorder and $-1 \leq J_1/J_0 < 0$ at strong disorder limit in Fig. 2.

The transition would accompany the crossover phenomenon which will be discussed in Sec. IV. Therefore, to better locate the phase transitions, we compute the localization length. The peaks of the localization length indicate the boundary of topological phase transitions [16,26]. Our numerical results show that the boundaries of the mean winding number match the peaks of localization length as denoted by the black crosses shown in Fig. 2. The critical disorder strength on the boundaries is denoted by U_c . Some examples of the localization length and the changes in mean winding numbers are given in Fig. 3. Figure 3(a) is a BI-TAI transition for $J_1 = 0$. Disorder drives the system directly to $w = 2$ because there is no singlet pairing between nearest neighbors for this Hamiltonian. When J_1 is nonzero, disorder drives the formation of singlet pairing between the nearest neighbor and the transition goes from $w = 0$ to $w = 1$. This result shows that weak disorder scattering changes topological properties of the system by strengthening the lowest-order nonzero intercell coupling. Figures 3(b) and 3(c) are TI-TAI transitions. Disorder drives the transition between different topological phases and eventually to normal insulating phase at extremely strong disorder. The change of the mean winding number is 1, meaning only one pair of edge states is removed or formed at a time. The second and third peaks are smaller, indicating that the delocalization at transition is rather weak in the strong disorder regime.

The scaling functions of the fluctuation of the winding number, denoted as Δw , for TAI phase is studied. The exponential convergence of Eq. (7) is shown by the rigorous mathematical proof in Ref. [27]. Figure 4(a) shows that Δw can be fit with e^{-cL}/L with $c = 0.0003$ (orange solid line in the figure). For the range of length considered, the exponential decay is not obvious; thus the decay is close to the algebraic (L^{-1}) decay, as shown by the green dashed line in Fig. 4(a). The scaling shows that Δw vanishes smoothly and w reaches exact quantization in the thermodynamic limit ($L \rightarrow \infty$). Moreover, to further examine the insulating phases, mean conductance as a function of chain length was computed. The details about the computation of conductance is described in the Appendixes. Figure 4(b) shows that the conductance exponentially decays with chain length, i.e., $G \propto e^{-L/\lambda}$, confirming the insulating behavior in the TAI phases. The numerical results agree with the two-parameter renormalization group theory [10,11], which states that both the mean conductance and the mean winding number converge exponentially in the thermodynamic limit.

The disorder drives not only the phase transition but also the crossover phenomenon. The latter can be seen by studying the probability distributions of wave functions. Moreover, in topological phases, the bulk-edge correspondence predicts that the numbers of pairs of edge states are the same as winding numbers [28,29]. We plot the disorder averaged probability density, projected to each sublattice, of the states near the band center. Figures 5(a) and 5(b) show the probability

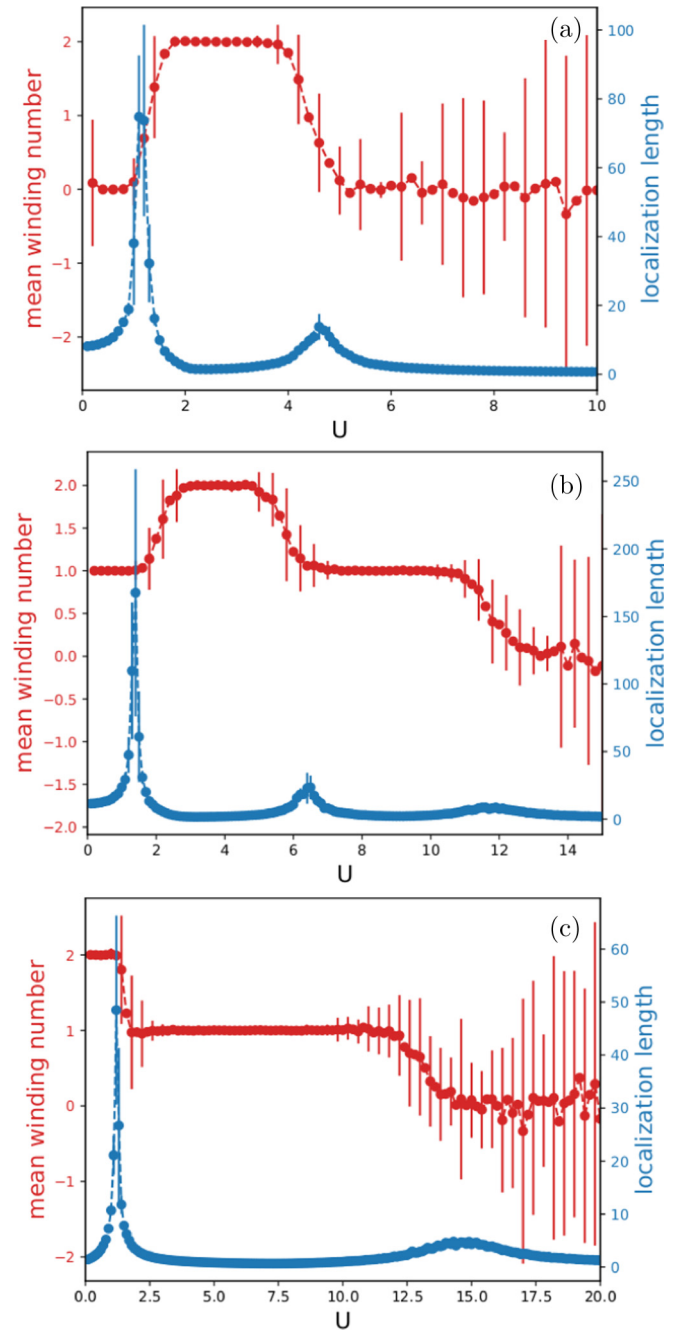


FIG. 3. Mean winding number and localization length as a function of disorder strength for (J_0, J_1, J_2) . (a) $(1, 0, -0.94)$; (b) $(1, -0.8, -1.74)$; (c) $(1, 2.4, 1.46)$. For the mean winding number, the error bars are plotted every other data point for clarity. The number of disorder configuration for the mean winding number and localization length is 50 and 10, respectively. The system length for winding number is 1000. The iteration steps for calculating the localization length is 10^4 that ensures convergence.

density near the band center for TAI phases with $w = 2$ via BI-TAI and TI-TAI transitions, respectively. The probability densities were obtained from direct diagonalization for a chain with length 1000 lattice sites. The 998th to 1001th states are plotted in each row and the corresponding energy is shown in the legend. The disorder strength increases from the left

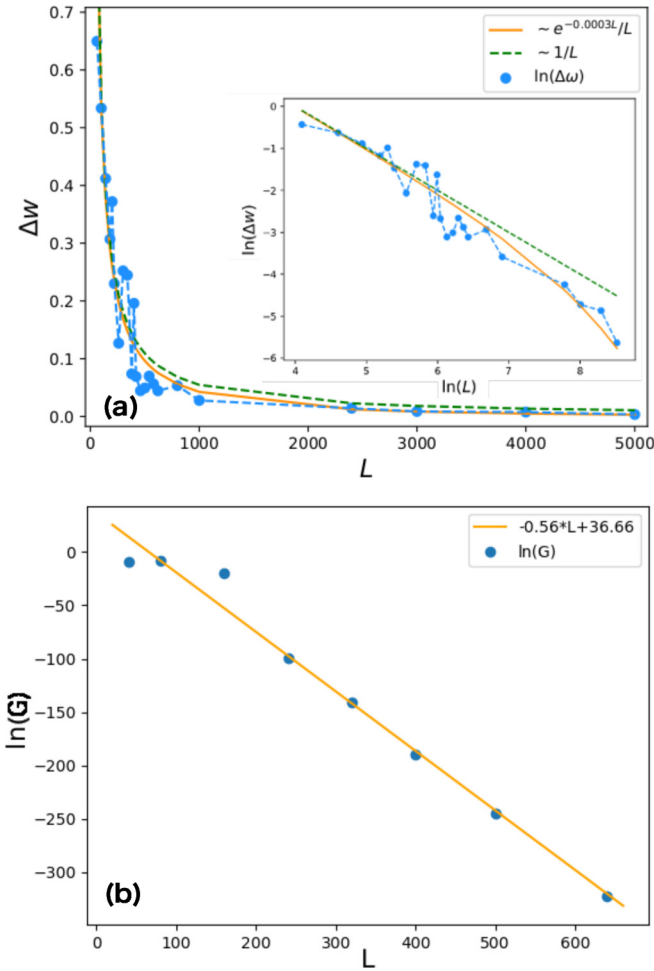


FIG. 4. (a) Scaling function of Δw for $(J_0, J_1, J_2) = (1, 0, -0.94)$ and $U = 2.5$. The inset shows the log-log plot. The dotted dashed lines are the numerical values. Panel (b) shows the scaling of the dimensionless conductance with chain length for the same parameters. The straight line is the fitted linear relation between $\ln(G)$ vs L .

to the right column. We find that the center column is in the crossover regions for $U^* < U < U_c$ and the rightmost column is in the TAI phase for $U > U_c$. The quantity U^* is the disorder strength in which the imaginary part of self-energy starts to be nonzero in the renormalized SSH system. U^* is labeled by the dashed line (red) in Fig. 2. In the crossover regions, the system transits from bulk insulator ($U = 0$) to AI ($U^* < U < U_c$) and then becomes TAI ($U > U_c$). Figure 5(a) shows the probability density along the $w = 0 \rightarrow 2$ transition. The leftmost column ($U = 0$) shows the probability density in the clean limit, where the states near the band center are bulk states and are away from zero energy. The rightmost column is the probability density at $U = 3 > U_c$, which is in the TAI phase with $w = 2$. There are two pairs of edge states at $E = 0$ —the same as the winding number.

On the other hand, Fig. 5(b) gives the probability density along the $w = 1 \rightarrow 2$ transition (TI-TAI transition). There is one pair of edge states at $E = 0$ in the clean limit, as shown in the leftmost column ($U = 0$). In the crossover region ($U^* < U < U_c$), the bulk states become Anderson localized states.

Interestingly, the edge state is not significantly affected by the disorder. The rightmost column is the probability density at $U = 3 > U_c$, which is in the TAI phase with $w = 2$. There are two pairs of edge states at $E = 0$, as expected by the bulk-edge correspondence. The bulk-edge correspondence for TAI phase with $w = 1$ is also satisfied. The probability density along the $w = 0 \rightarrow 1$ and $w = 2 \rightarrow 1$ transitions are presented in Fig. 6. In Fig. 6(b), the winding number decreases from the clean limit to TAI phase. In the crossover region, as shown in the center column, the probability density gains few bulk contributions, indicating the robustness of edge states. In the TAI phase with $w = 1$, as shown in the rightmost column, only one pair of edge state is left at zero energy, while the other pair is scattered into bulk with a higher energy level.

In short, to demonstrate the crossover, the probability density in different regimes is plotted in Figs. 5 and 6. In Figs. 5(a), 5(b) and Fig. 6(a), the winding number increases from the clean limit to TAI phase. The probability density in crossover regions is shown in the center column. The energy levels are drawn nearer to $E_f = 0$ than that in the clean limit. The spikes in the probability density demonstrate the wave function localization in the bulk.

In the finite SSH system, it is shown that the phase transition accompanies the crossover phenomenon. Nevertheless, in the thermodynamic limit, the crossover phenomenon should appear when the imaginary part of self-energy starts to be nonzero in the renormalized SSH system. This is because the nonzero value of the imaginary part of self-energy would result in the broadening of Fermi level (as well as energy band) and depicts more localized states near the zero energy. In this sense, when the energy band shift and the broadening of Fermi level together close the band gap, the corresponding disorder strength for the closure of the band gap would be the critical disorder strength. In Sec. IV, we calculate the self-energy and the critical disorder strength by using Born approximation and compare the results with the finite SSH system.

IV. SELF-ENERGY AND BAND CLOSURE

As shown in Sec. III, before the phase transitions, there are crossover regions, where Anderson localization starts to come into play [10,11]. This is the crossover regime when the BI (TI) enters the AI (TAI) phases before phase transition. Within crossover, the topological edge states do not significantly change while the density of states penetrate into the energy gap. The energy shift and Fermi level broadening by disorder could close the band gap. In this sense, the crossover phenomenon in the finite SSH system corresponds to the nonzero imaginary part of self-energy. Furthermore, the closure of the band gap can be used to determine the critical disorder strength. We consider two approximations: first Born approximation (FBA) and self-consistent Born approximation (SCBA). The self-energy Σ is given by the self-consistent equation

$$\Sigma = \frac{U^2}{12} \sum_{k \in \text{BZ}} \frac{1}{z - H_0(k) - \Sigma}, \quad (9)$$

where $z = E_f + i\eta$. By regarding the self-energy as $\Sigma = \Sigma_x \sigma_x + \Sigma_0 \sigma_0$ (which is consistent with the numerical result),

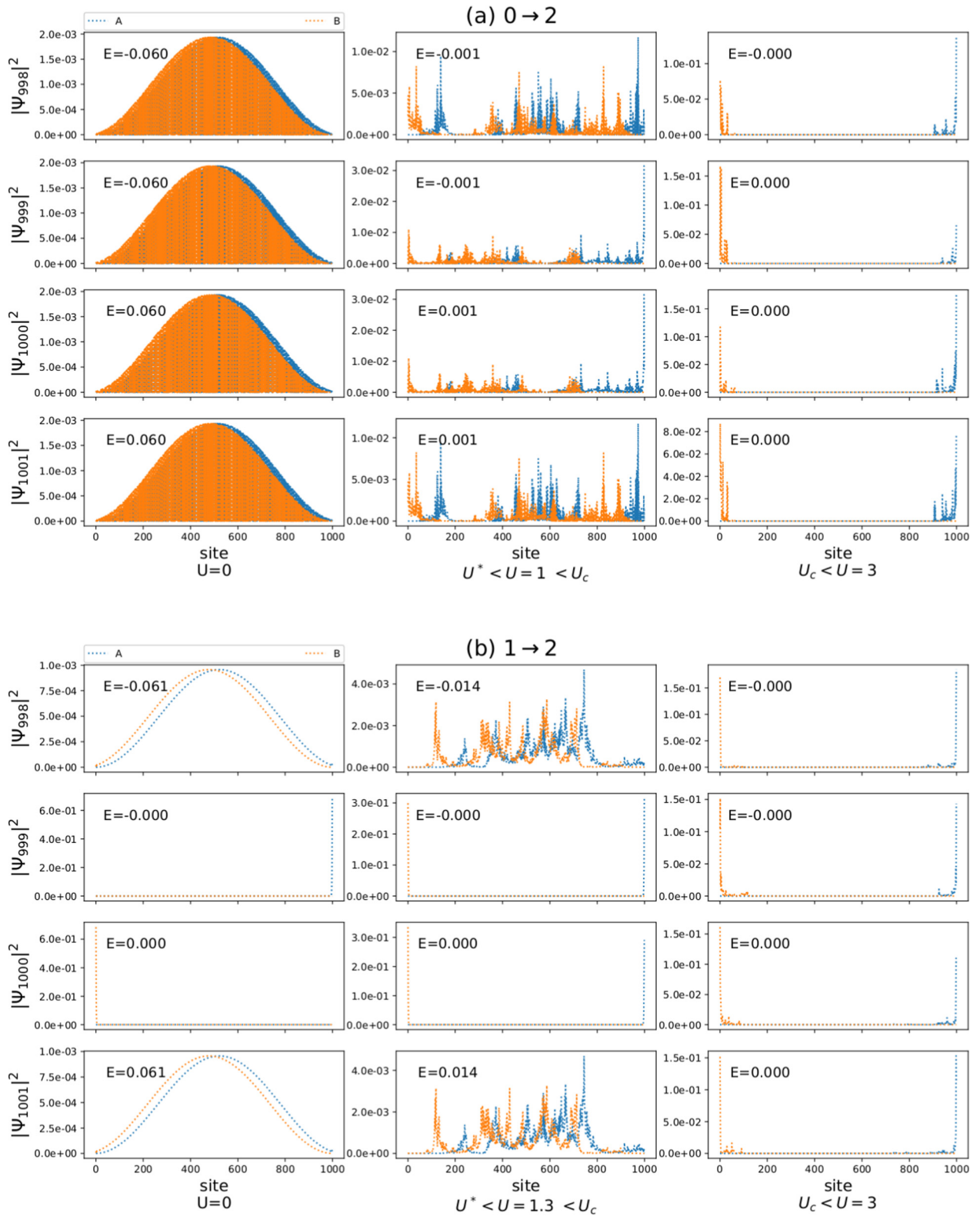
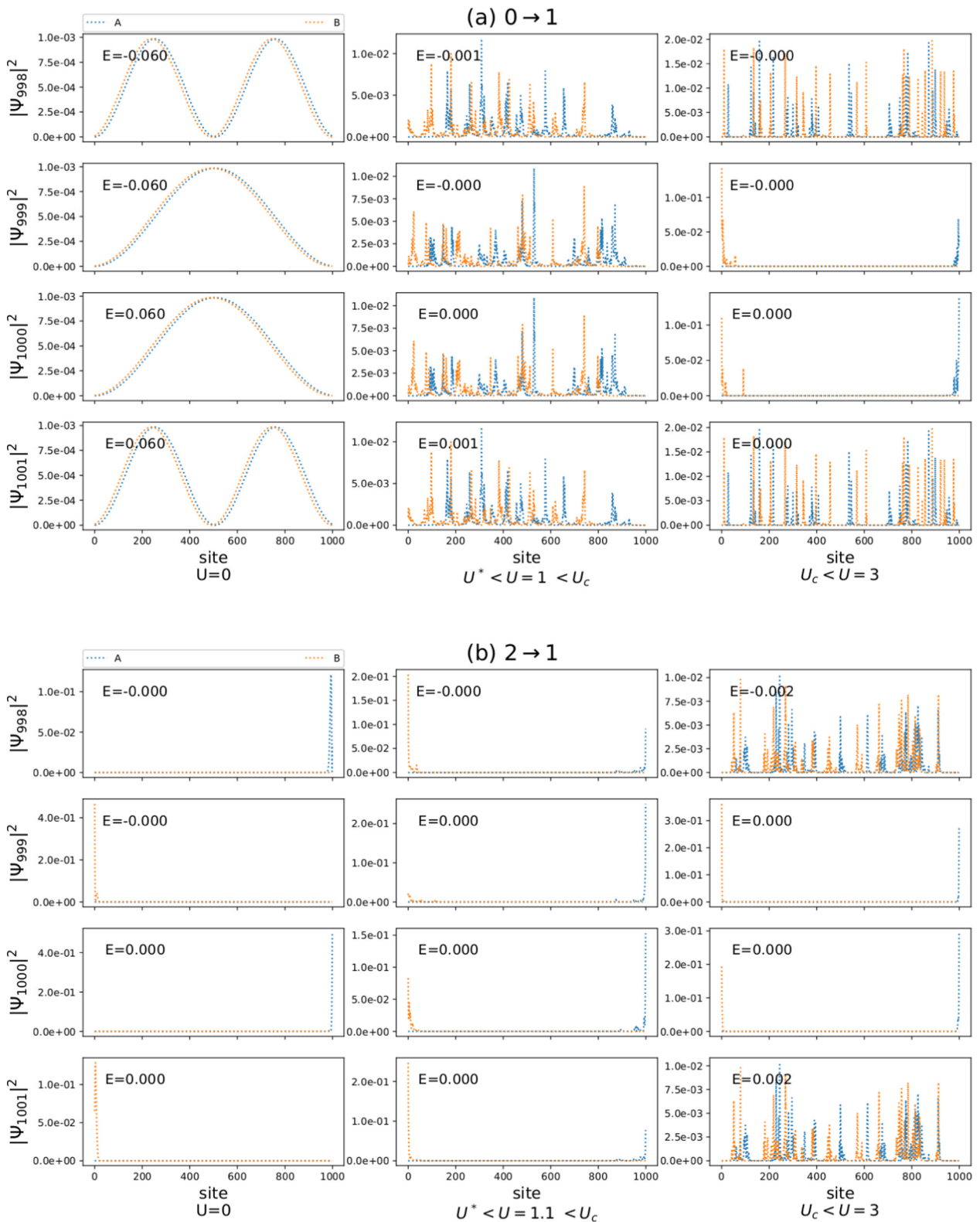


FIG. 5. Numerical results showing the probability density for states near the band center in the clean limit (leftmost column), crossover (center column), and TAI phases (rightmost column) for (J_0, J_1, J_2) . (a) $(1, 0, -0.96)$ with $U^* = 0.7$ and $U_c = 1.1$ and (b) $(1, -0.8, -1.74)$ with $U^* = 1.2$ and $U_c = 1.4$. The number of disorder configuration is 20. The length of the chain is 1000.



it can be shown that Eq. (9) can be written as the renormalized \bar{J}_0 and \bar{E}_f through the definitions $\bar{J}_0 = J_0 + \Sigma_x$ and $\bar{E}_f = E_f - \Sigma_0$. We have

$$\bar{J}_0 = J_0 - \frac{U^2}{12} \sum_{k \in \text{BZ}} \frac{\bar{J}_0 + c_k}{(\bar{J}_0 + c_k^2)^2 + s_k^2 - (\bar{E}_f + i\eta)^2} \quad (10)$$

and

$$\bar{E}_f = E_f + \frac{U^2}{12} \sum_{k \in \text{BZ}} \frac{\bar{E}_f + i\eta}{(\bar{J}_0 + c_k^2)^2 + s_k^2 - (\bar{E}_f + i\eta)^2}, \quad (11)$$

where $c_k = J_1 \cos(k) + J_2 \cos(2k)$ and $s_k = J_1 \sin(k) + J_2 \sin(2k)$, where the lattice constant is taken to be 1. The summation can be replaced by the integral, i.e., $\sum_{k \in \text{BZ}} = (1/2\pi) \int_{-\pi}^{\pi} dk$. The self-energy can be solved analytically as given in the Appendixes.

In FBA, $\delta J_0 = \bar{J}_0 - J_0$ and $\delta E_f = \bar{E}_f - E_f$ are evaluated independently. At half-filling, i.e., $E_f = 0$, δE_f is zero at weak disorder. The vanishing δE_f implies that no crossover regions can be identified. The energy dispersion becomes $E = \pm \sqrt{(h_x + \delta J_0)^2 + h_y^2}$. The condition for the gap closure is then given by

$$\begin{aligned} J_0 + \delta J_0 + J_1 \cos k_0 + J_2 \cos(2k_0) &= 0, \\ J_1 \sin k_0 + J_2 \sin(2k_0) &= 0. \end{aligned} \quad (12)$$

For $k_0 = \pi$, one obtains the critical disorder strength in FBA denoted as U_c^{FBA} by equating

$$E_{\min} = \frac{(U_c^{\text{FBA}})^2}{24J_0}, \quad (13)$$

where E_{\min} is the lowest energy of the conduction band in the clean limit. For $1.8 \leq J_1/J_0 \leq 2.2$, the band minima shift away from π ; to estimate U_c^{FBA} for comparison with U_c , Eq. (13) is applied even though Eq. (12) is not satisfied. The critical disorder strength U_c^{FBA} found by this criterion is drawn on Fig. 7(a) with stars (\star) and open circles (\circ). We find that U_c^{FBA} exhibits approximately a straight line phase boundary ($U_c^{\text{FBA}} \approx 1.2$). For stronger $U_c > 1.2$, U_c^{FBA} cannot qualitatively fit the results of U_c . E_{\min} varies only in the regime $1.8 \leq J_1/J_0 \leq 2.2$ and is a constant beyond this regime; U_c^{FBA} follows the same trend as the bare values of E_{\min} according to Eq. (13). The overall band closure boundary within FBA is qualitatively different from the phase transition boundary.

In contrast to FBA, SCBA gives rise to the pure imaginary part δE_f , which also affects δJ_0 in the self-consistent calculation. The numerical results show that the self-energy has two components $\Sigma = \delta J_0 \sigma_x + \delta E_f \sigma_0$. Within SCBA, δE_f acquires a nonzero imaginary part, indicating the appearance of midgap states. The corresponding disorder strength (U^*) is labeled by the dashed line (red) in the phase diagram (see Fig. 2). At band closure, the energy gap is filled with electronic states when the band gap is renormalized by δJ_0 and smeared out by the Fermi level broadening in the presence of disorder. Thus the critical disorder strength U_c^{SCBA} is determined by

$$\sqrt{[h_x(k_0) + \delta J_0]^2 + h_y(k_0)^2} - |\delta E_f| = 0 \quad (14)$$

and drawn on Fig. 7(a) with dots (\bullet). We find that U_c^{SCBA} gives a qualitative description of the phase transition boundary (U_c).

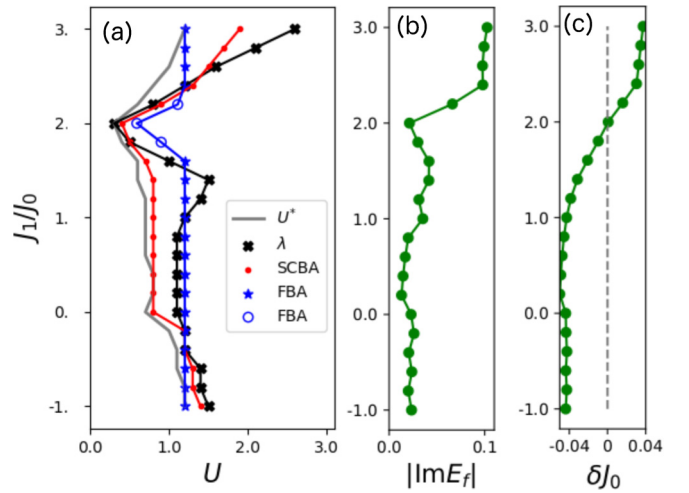


FIG. 7. (a) Numerical results showing the boundaries for band closure determined by SCBA (red \bullet) and FBA (blue \star). The critical disorder strength U_c is shown by the cross (black \times). The region $-1 \leq J_1/J_0 < 0$ is the transition $w = 1 \rightarrow 2$. $J_1/J_0 = 0$ is the transition $w = 0 \rightarrow 2$. The region $0 < J_1/J_0 < 2$ is the transition $w = 0 \rightarrow 1$. The region $2 \leq J_1/J_0 \leq 3$ is the transition $w = 2 \rightarrow 1$. The empty circles along the FBA boundary are given by Eq. (13) without satisfying Eq. (12). (b) The imaginary part of the self-energy at band closure. $\text{Im}E_f$ is always negative. (c) δJ_0 given by SCBA at band closure.

In the renormalized SSH system, the change in the winding number would be from the band shift and the localized state in the gap. The former is determined by the value of δJ_0 and the latter by the value $\text{Im}E_f$, which are shown in Figs. 7(b) and 7(c). From the numerical SCBA calculation, we find that δJ_0 changes sign. When δJ_0 is negative, the energy band minimum is pulled down, and the bulk states at zero energy become significant. Our numerical results show that U_c^{FBA} fits the trend with U_c in this regime. On the other hand, positive δJ_0 leads to the rise of the energy band minimum. In this case, our numerical results show that U_c^{SCBA} fits the trend with U_c better than U_c^{FBA} . For the case of vanishing δJ_0 , the change in zero mode of edge states is due to the broadening of Fermi level and, thus, U_c^{SCBA} agrees with U_c . Furthermore, the agreement between these values of U_c , U_c^{SCBA} , and U_c^{FBA} depends on the topological properties in the clean limit. For systems in the topological states in the clean limit, U_c^{SCBA} agrees with U_c phase boundary. We discuss these numerical results in detail in the following.

In the region $0 \leq J_1/J_0 < 1.8$, which is the BI-TAI transition ($0 \rightarrow 1$ and $0 \rightarrow 2$), FBA gives a quantitative agreement to the phase boundary, as shown in Fig. 7(a). In this region, δJ_0 is negative and large, and $|\text{Im}E_f|$ is small, indicating that the major contribution is from the band edge. At point $J_1/J_0 = 1.8$, the transition is also from $w = 0$ to $w = 1$, i.e., BI-TAI transition, but U_c^{SCBA} agrees with U_c better than U_c^{FBA} for this particular point. Since the renormalized band gap is not exactly zero within FBA, followed by the discussion along with Eqs. (12) and (13), U_c^{FBA} does not agree with U_c .

In the region $-1 \leq J_1/J_0 < 0$, which is the phase transition $w = 1 \rightarrow 2$, SCBA gives negative δJ_0 , suggesting that the extra zero mode edge states would be from bulk states. We

observe that U_c^{SCBA} is indeed quantitatively closer to U_c than U_c^{FBA} , especially in the region with stronger U_c . Only in the region with weaker U_c do we find that $U_c^{\text{FBA}} \approx U_c^{\text{SCBA}} \approx U_c$. In contrast to the BI-TAI transition, there exists zero mode edge states in the clean limit; U_c^{SCBA} dominates the phase boundary, as a consequence of the zero mode edge state being topologically protected up to all order of scattering diagram.

On the other hand, for the transition from high to low winding numbers ($2 \rightarrow 1$), i.e., the regime $J_1/J_0 \geq 2$, U_c^{SCBA} fits the trend of the U_c phase boundary better than U_c^{FBA} , as shown in Fig. 7(a). Figures 7(b) and 7(c) show that the Fermi level broadening becomes significant. This is in agreement with the probability density in finite system shown in the right-most column in Fig. 6(b). For reducing the winding number, one pair of the zero mode edge states is scattered into bulk. In contrast, FBA still gives zero Fermi level broadening and negative band shift δJ_0 , i.e., the bulk state dominates the phase transition. As mentioned above, U_c^{FBA} exhibits a straight line boundary $U_c^{\text{FBA}} \approx 1.2$. When $J_1/J_0 = 2.4$, U_c^{FBA} approaches the straight line boundary and numerically at this point we obtain $U_c^{\text{FBA}} \approx U_c^{\text{SCBA}}$.

As pointed out by Guo *et al.* [8] in their study of the three-dimensional TAI, the TAI regime where the self-energy obtains an imaginary part is the “true” TAI phase. In three-dimensional TAI, because bulk states do not contribute to conductance, bulk states must be localized. In one dimension, we find that band closure within SCBA gives a qualitative agreement with the phase transition boundary. It suggests that the interplay between the band edge renormalization and lifetime broadening is essential for the phase transition. Similar to the three-dimensional TAI, we find that, in all TAI phases, the self-energy has a nonzero imaginary part, confirming the TAI phases. Nonetheless, we show that, for high-to-low transition, the TAI phase has significantly larger lifetime broadening.

V. CONCLUSION

We have shown that the higher winding numbers exhibit in the Su-Schrieffer-Heeger (SSH) system when the second nearest-neighbor hopping is included in the SSH

Hamiltonian. We study the transition between bulk insulator (BI), topological insulator (TI), and topological Anderson insulator (TAI). In the presence of disorder, topological phase transitions driven by disorder are identified by the divergence of localization length. The disorder-induced phases are further investigated by the mean winding numbers and wave functions. The scaling of the mean winding number is reported. We calculated the critical disorder strength by using first Born approximation (FBA) and self-consistent Born approximation (SCBA). The critical disorder strength for transitions are calculated by the criterion of the closure of energy gap resulting from the broadening of energy band and Fermi level. Compared to the phase boundary given by delocalization (U_c), we showed that the FBA exhibits phase boundary closer to U_c than the SCBA for BI-TAI transition if the renormalized band gap is zero within FBA. For TI-TAI transition, we also showed the phase boundary obtained from SCBA qualitatively fits U_c . Moreover, SCBA shows that, for the transition from low-to-high winding number, the band shift is more dominant, while for high-to-low winding number, the Fermi level broadening is more significant.

ACKNOWLEDGMENTS

We would like to thank D. W. Chiou for useful discussions on the winding number. The authors acknowledge the financial support by the Ministry of Science and Technology of Taiwan through Grants No. MOST 108-2112-M-004-002-MY2 (H.C.H.) and No. MOST 108-2112-M-110-009 (T.W.C.).

APPENDIX A: ANALYTICAL CALCULATION OF BORN APPROXIMATION

Equations (10) and (11) can be evaluated analytically. The result of Eq. (10) is given by (let $\eta \rightarrow 0$)

$$\bar{J}_0 = J_0 - \frac{U^2}{12} \frac{1}{2\bar{J}_0} \left\{ 1 + (-i) \frac{\sqrt{2}}{2} \left[\frac{1}{\Gamma_1} - \frac{1}{\Gamma_2} \right] \right\}, \quad (\text{A1})$$

where

$$\begin{aligned} \frac{1}{\Gamma_1} &= \frac{J_2 [2\bar{J}_0^3 + \bar{J}_0(2\bar{E}_f - J_1^2 - 2J_2^2) + J_1(J_1J_2 + \sqrt{\mu_1})]}{\sqrt{\mu_1}\sqrt{M_1}}, \\ \frac{1}{\Gamma_2} &= \frac{J_2 [-2\bar{J}_0^3 + \bar{J}_0(-2\bar{E}_f + J_1^2 + 2J_2^2) + J_1(-J_1J_2 + \sqrt{\mu_1})]}{\sqrt{\mu_1}\sqrt{M_2}}, \end{aligned} \quad (\text{A2})$$

and

$$\begin{aligned} \mu_1 &= -4\bar{J}_0^3 J_2 + J_1^2 J_2^2 - 2\bar{J}_0 J_2 (-2\bar{E}_f + J_1^2 + 2J_2^2) + \bar{J}_0^2 (J_1^2 + 8J_2^2), \\ M_1 &= 2\bar{J}_0^3 J_2 - \bar{J}_0^2 (J_1^2 - 4J_2^2) - J_1 J_2 (J_1 J_2 + \sqrt{\mu_1}) - \bar{J}_0 (2\bar{E}_f J_2 - 2J_2^3 + J_1 \sqrt{\mu_1}), \\ M_2 &= 2\bar{J}_0^3 J_2 - \bar{J}_0^2 (J_1^2 - 4J_2^2) + J_1 J_2 (-J_1 J_2 + \sqrt{\mu_1}) + \bar{J}_0 (-2\bar{E}_f J_2 + 2J_2^3 + J_1 \sqrt{\mu_1}). \end{aligned} \quad (\text{A3})$$

In the Born approximation (not self-consistent), \bar{J}_0 and \bar{E}_f are replaced by the bare values J_0 and E_f at the right hand side of the equality of Eq. (A1). In this case, the second term in $\{\dots\}$

of Eq. (A1) is pure imaginary and we have

$$\delta J_0 \equiv -|E| = \text{Re}[\bar{J}_0] - J_0 = -\frac{U^2}{24J_0}. \quad (\text{A4})$$

On the other hand, Eq. (11) can also be evaluated analytically, and the result is

$$\bar{E}_f = E_f + (-i)\frac{U^2}{12}\bar{E}_f\sqrt{2}\left(\frac{1}{\Gamma_3} + \frac{1}{\Gamma_4}\right), \quad (\text{A5})$$

where

$$\frac{1}{\Gamma_3} = \frac{\bar{J}_0 J_2}{\sqrt{\mu_1}\sqrt{M_1}}, \quad \frac{1}{\Gamma_4} = \frac{\bar{J}_0 J_2}{\sqrt{\mu_1}\sqrt{M_2}}. \quad (\text{A6})$$

In the Born approximation, \bar{E}_f is replaced by E_f at the right hand side of Eq. (A5). Furthermore, in this approximation, when $E_f = 0$, we have $\bar{E}_f = 0$.

APPENDIX B: CALCULATION OF THE CONDUCTANCE

To compute the length scaling of conductance, the Landauer-Buttiker formula for two-terminal transport was utilized. The conductance is related to the transmission function (T) by $(e^2/h)T$. The transmission function is given by [30]

$$T = \text{Tr}[\Gamma_l G_{1L}^R \Gamma_r G_{1L}^A], \quad (\text{B1})$$

where $G_{1L}^{R(A)}$ is the retarded (advanced) Green's function corresponding to the transmission from the first to the last site of the chain and $\Gamma_{l(r)}$ is the surface self-energy of the left (right) lead. The normal metal lead is attached to each end of the SSH chain of various length (L). The dispersion of the leads are taken to be $E = -2t_l \cos(ka)$, where $t_l = 2$, $a = 1$ and k is the wave vector.

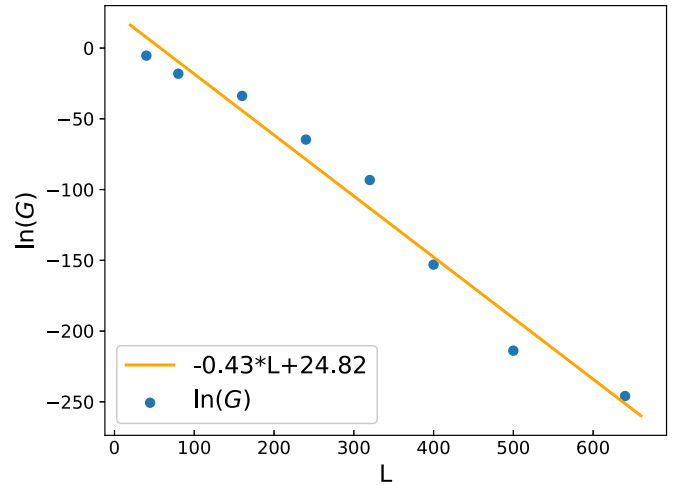


FIG. 8. Scaling of the conductance with chain length for TAI phase for $(J_0, J_1, J_2) = (1, -0.8, -1, 76)$ and $U = 3.5$.

According to the theory of localization [31], the scaling function for the dimensionless conductance, denoted by G , is given by $\beta(G) = d \ln(G)/d \ln(L)$. By chain rule,

$$\beta(G) = \frac{d \ln(G)}{dL} \frac{dL}{d \ln(L)} = L \frac{d \ln(G)}{dL}. \quad (\text{B2})$$

In the limit of strong disorder, the conductance is assumed to be proportional to $e^{-L/\lambda}$, where L is the system length and λ is the localization length. Figure 8 shows one example of the conductance scaling of TAI regime [point (a) in Table I]. The orange line in the plot is the fitted linear relation between $\ln(G)$ and L . The scaling shows that conductance exponentially decays with the system length and confirms the insulating behavior in TAI phases.

-
- [1] P. W. Anderson, *Phys. Rev.* **109**, 1492 (1958).
[2] E. Abrahams, P. W. Anderson, D. C. Licciardello, and T. V. Ramakrishnan, *Phys. Rev. Lett.* **42**, 673 (1979).
[3] E. Abrahams, *50 Years of Anderson Localization* (World Scientific, Singapore, 2010).
[4] J. Billy, V. Joose, Z. Zuo, A. Bernard, B. Hambrecht, P. Lugan, D. Clement, L. Sanchez-Palencia, P. Bouyer, and A. Aspect, *Nature (London)* **453**, 891 (2008).
[5] R. Du, H.-C. Hsu, A. C. Balram, Y. Yin, S. Dong, W. Dai, W. Zhao, D. S. Kim, S.-Y. Yu, J. Wang *et al.*, *Phys. Rev. B* **93**, 195402 (2016).
[6] J. Li, R.-L. Chu, J. K. Jain, and S.-Q. Shen, *Phys. Rev. Lett.* **102**, 136806 (2009).
[7] C. W. Groth, M. Wimmer, A. R. Akhmerov, J. Tworzydło, and C. W. J. Beenakker, *Phys. Rev. Lett.* **103**, 196805 (2009).
[8] H.-M. Guo, G. Rosenberg, G. Refael, and M. Franz, *Phys. Rev. Lett.* **105**, 216601 (2010).
[9] D. Xu, J. Qi, J. Liu, V. Sacksteder, X. C. Xie, and H. Jiang, *Phys. Rev. B* **85**, 195140 (2012).
[10] A. Altland, D. Bagrets, L. Fritz, A. Kamenev, and H. Schmiedt, *Phys. Rev. Lett.* **112**, 206602 (2014).
[11] A. Altland, D. Bagrets, and A. Kamenev, *Phys. Rev. B* **91**, 085429 (2015).
[12] N. M. Gergs, L. Fritz, and D. Schuricht, *Phys. Rev. B* **93**, 075129 (2016).
[13] E. J. Meier, F. A. An, A. Dauphin, M. Maffei, P. Massignan, T. L. Hughes, and B. Gadway, *Science* **362**, 929 (2018).
[14] D. Xie, W. Gou, T. Xiao, B. Gadway, and B. Yan, *npj Quantum Inf.* **5**, 55 (2019).
[15] Z. Fedorova (Cherpakova), C. Jorg, C. Dauer, F. Letscher, M. Fleischhauer, S. Eggert, S. Linden, and G. von Freymann, *Light Sci. Appl.* **8**, 63 (2019).
[16] I. Mondragon-Shem, T. L. Hughes, J. Song, and E. Prodan, *Phys. Rev. Lett.* **113**, 046802 (2014).
[17] C. G. Velasco and B. Paredes, *Phys. Rev. Lett.* **119**, 115301 (2017).
[18] M. Maffei, A. Dauphin, F. Cardano, M. Lewenstein, and P. Massignan, *New J. Phys.* **20**, 013023 (2018).
[19] B. Pérez-González, M. Bello, A. Gómez-León, and G. Platero, *Phys. Rev. B* **99**, 035146 (2019).
[20] X. Liu, H.-C. Hsu, and C.-X. Liu, *Phys. Rev. Lett.* **111**, 086802 (2013).
[21] H.-C. Hsu, X. Liu, and C.-X. Liu, *Phys. Rev. B* **88**, 085315 (2013).
[22] R. Bianco and R. Resta, *Phys. Rev. B* **84**, 241106(R) (2011).

- [23] C. H. Lewenkopf and E. R. Mucciolo, *J. Comput. Electron.* **12**, 203 (2013).
- [24] A. MacKinnon and B. Kramer, *Z. Phys. B: Condens. Matter* **53**, 1 (1983).
- [25] B. Kramer and A. MacKinnon, *Rep. Prog. Phys.* **56**, 1469 (1993).
- [26] A. Habibi, S. A. Jafari, and S. Rouhani, *Phys. Rev. B* **98**, 035142 (2018).
- [27] E. Prodan, *Appl. Math. Res. Express* **2013**, 176 (2012).
- [28] A. Kitaev, *Periodic Table for Topological Insulators and Superconductors*, AIP Conf. Proc. No. 1134 (AIP, Melville, NY, 2009), p. 22.
- [29] B.-H. Chen and D.-W. Chiou, *Phys. Lett. A* **384**, 126168 (2020).
- [30] S. Datta, *Electronic Transport in Mesoscopic Systems* (Cambridge University Press, Cambridge, UK, 1997).
- [31] J. Rammer, *Quantum Transport Theory*, Frontiers in Physics (Avalon Publishing, New York, 2004).